

Pro-Oxidant Therapeutic Activities of Cerium Oxide Nanoparticles in Colorectal Carcinoma Cells

Aparna Datta,* Snehasis Mishra, Krishnendu Manna, Krishna Das Saha, Siddhartha Mukherjee, and Somenath Roy



Cite This: <https://dx.doi.org/10.1021/acsomega.9b04006>



Read Online

ACCESS |



Metrics & More

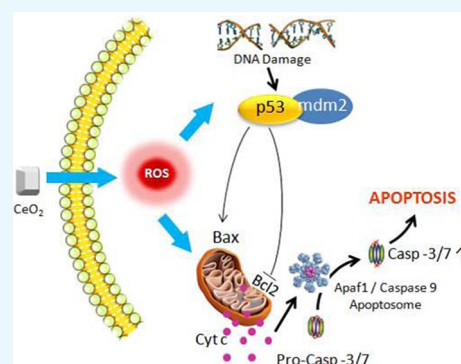


Article Recommendations



Supporting Information

ABSTRACT: Given that basal levels of reactive oxygen species (ROS) are higher in cancer cells, there is a growing school of thought that endorses pro-oxidants as potential chemotherapeutic agents. Intriguingly, cerium oxide (CeO_2) nanoparticles can manifest either anti- or pro-oxidant activity as a function of differential pH of various subcellular localizations. In an acidic pH environment, for example, in extracellular milieu of cancer cells, CeO_2 would function as a pro-oxidant. Based on this concept, the present study is designed to investigate the pro-oxidant activities of CeO_2 in human colorectal carcinoma cell line (HCT 116). For comparison, we have also studied the effect of ceria nanoparticles on human embryonic kidney (HEK 293) cells. Dose-dependent viability of cancerous as well as normal cells has been assessed by treating them independently with CeO_2 nanoparticles of different concentrations (5–100 $\mu\text{g}/\text{mL}$) in the culture media. The half maximal inhibitory concentration (IC_{50}) of nanoceria for HCT 116 is found to be 50.48 $\mu\text{g}/\text{mL}$ while that for the HEK 293 cell line is 92.03 $\mu\text{g}/\text{mL}$. To understand the intricate molecular mechanisms of CeO_2 -induced cellular apoptosis, a series of experiments have been conducted. The apoptosis-inducing ability of nanoceria has been investigated by Annexin V-FITC staining, caspase 3/9 analysis, cytochrome *c* release, intracellular ROS analysis, and mitochondrial membrane potential analysis using flow cytometry. Experimental data suggest that CeO_2 treatment causes DNA fragmentation through enhanced generation of ROS, which ultimately leads to cellular apoptosis through the p53-dependent mitochondrial signaling pathway.



INTRODUCTION

Free-radical-induced oxidative injury is considered to be the fundamental mechanism underlying several human diseases such as neurodegenerative diseases, cancer, stroke, and numerous other ailments. Owing to its potential to prevent, delay, or ameliorate the physiological disorders caused or aggravated by ROS, antioxidant therapy is of enormous clinical interest.¹ Although a gamut of preclinical *in vitro* and animal data suggest inverse associations between antioxidants and the risk of various cancers, clinical trial results are not convincing enough in many cases, especially in the setting of chronic preventative therapy.^{2,3} Hence, the need of the hour is to focus on designing more disease-specific, target-directed, and highly bioavailable therapeutics, along with the choice of optimal treatment times and durations.

In view of the aberrant redox status of cancer cells, the current treatment regimen relies on pro-oxidant therapies, which is efficacious in selectively inducing cancer cell death *via* oxidative stress, while sparing the “normal cells.” Cancer cells, because of a loss in proper redox control, exhibit an elevated level of ROS production, as compared to healthy cells.⁴ Pro-oxidant chemotherapeutic agents induce additional oxidative stress in cancer cells, thereby driving them into apoptotic cell death. A similar level of oxidative stress induced by the pro-

oxidants, when administered in a calibrated dose, would not cross the apoptotic threshold in normal cells.⁵ Therefore, controlled enhancement of intracellular ROS production, below cytotoxic threshold, by the use of pro-oxidative substances is instrumental in cancer treatment.

With the emergence of nanomedicine, nanoparticles are being extensively investigated as potential cargos for delivery of therapeutic drugs to specific cellular targets or organs, for example, to mitochondria⁶ or to the brain.⁷ Nanoparticles, with inherent pharmacological attributes, are gaining special attention because of their tremendous potential in anticancer therapy. By virtue of their redox-modulatory and enzyme-like activities, cerium oxide (CeO_2) nanoparticles are envisaged as promising candidates in nanomedicine. Ceria nanoparticles have been shown to act as catalysts that mimic a series of redox enzymes, including superoxide dismutase, catalase, peroxidase, phosphotriesterase, phosphatase, and oxidase, which can

Received: November 25, 2019

Accepted: April 8, 2020

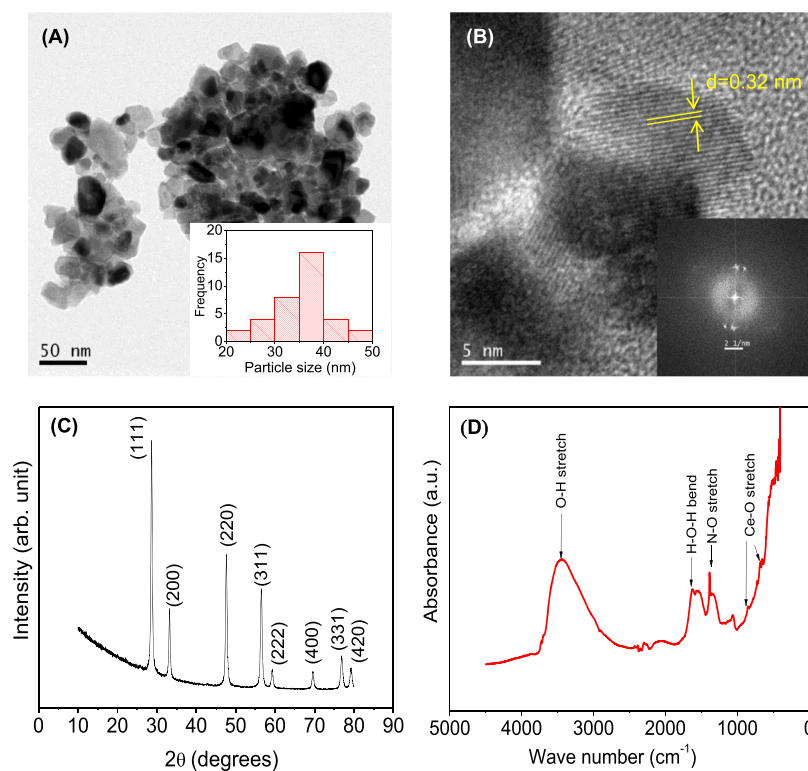


Figure 1. (A) TEM image of the CeO₂ nanoparticles; (B) HRTEM image of the nanoparticles with pronounced lattice fringes, inset: corresponding FFT pattern; and (C) XRD spectra for CeO₂ nanoparticles. Manifestation of the {111} plane is apparent from the relative intensities of the XRD peaks; (D) FTIR spectra of pristine CeO₂ nanoparticles.

scavenge reactive oxygen species (ROS).^{8–14} The enzyme-mimicking activities of CeO₂ for free-radical scavenging, have been ascribed to the auto-regenerative cycle of Ce³⁺/Ce⁴⁺ and oxygen vacancies on the surface of ceria.¹⁵ Recent studies demonstrating the neuroprotective and cardioprotective roles of CeO₂ nanoparticles have been correlated with its antioxidative and redox-modulatory activities.^{16,17} On the other hand, nanoceria have been found to produce significant oxidative stress in human bronchoalveolar carcinoma and¹⁸ human hepatocellular carcinoma.¹⁹ In the case of lung adenocarcinoma (A549) cells, CeO₂ increases the production of ROS which leads to a decrease in the antioxidant level of cells and apoptotic cell death.²⁰ The elevated levels of ROS also cause damage to DNA and halts cell cycle progression. Studies have also shown that co-treatment with ceria nanoparticles and radiation therapy caused significant activation of c-Jun terminal kinase, a key driver of radiation therapy-induced apoptosis, in human pancreatic cancer cells.²¹ Intriguingly, cytotoxicity and genotoxicity of CeO₂ is preferential to cancer cells, whereas inverse effects are observed for healthy cells. For example, more than two-fold increase in radiation-induced ROS production was observed in human pancreatic cancer cells (L3.6pl) treated with 10 μM ceria nanoparticles for 24 h, while a similar treatment led to a constant decrease (>50%) in radiation-induced ROS production for normal pancreatic cells (hTERT-HPNE).²² Selective cytoprotection provided by nanoceria to normal cells, but not to cancer cells, during oxidative stress may be explained by the pH-dependent oxidation state of the material. It is observed that CeO₂ exhibits optimal antioxidative properties at physiological pH, whereas it behaves as an oxidase at acidic pH.¹⁴ Noticeably, in solid tumors, the preferential dependence

of cancer cells on glycolysis (Warburg effect) leads to a lowering of tumor cell pH.²³ In acidic environments, CeO₂ favors the scavenging of superoxide radicals over the hydrogen peroxide, resulting in accumulation of the latter whereas in neutral pH (healthy cells), ceria scavenges both.¹⁹ Nonetheless, the multimechanistic nature of the ceria-mediated modulation of intracellular ROS ratifies the rationale for its extensive exploration in cancer therapy.

The present study is aimed to understand the molecular mechanism underlying the toxicity of CeO₂ nanoparticles on human colorectal carcinoma cell line (HCT 116). The cancer cells have been treated with different concentrations of pristine nanoceria, synthesized using a chemical precipitation method. Owing to the nontrivial influence of surface defects and oxygen vacancies on the ROS modulating properties of CeO₂, we refrained from capping the nanoparticle surface with surfactants or organic molecules, which can potentially inhibit a set of pro-oxidant biological effects. As indicators of apoptosis, DNA fragmentation, activation of caspase-3 and caspase-9, as well as Bcl-2 expression has been explored. To understand the molecular mechanism of ceria-induced oxidative stress, a plethora of *in vitro* toxicity indices have been conducted, focusing on the involvement of the death-responsive cellular mechanism.

RESULTS AND DISCUSSION

Characterization of CeO₂ Nanoparticles. Morphological characterization of pristine CeO₂ nanoparticles was performed by transmission electron microscopy (TEM). Figure 1A presents clusters of pristine CeO₂ nanoparticles, the majority of which are in the range of 30–40 nm. The tendency of pristine CeO₂ to form clusters on the TEM grid could be

scribed to a low zeta potential (-4.9 mV) of the pristine nanoparticles in aqueous medium. The intrinsic presence of hydroxyl ions on the particle surface would facilitate the formation of hydrogen bond between particles, resulting in soft aggregation. High-resolution TEM (HRTEM) (Figure 1B) reveals the lattice fringes with the d -spacing of 0.32 nm, which could be indexed to the (111) plane of ceria. The value of interplanar spacing is in agreement with the fast Fourier transform (FFT) calculations (inset of Figure 1B). The X-ray diffraction (XRD) pattern of pristine ceria nanoparticles is shown in Figure 1C in the 2θ range of 25 – 80° . All of the discernible peaks could be indexed to a pure cubic (fluorite) structure of CeO_2 (space group: $Fm\bar{3}m$) with a lattice constant $a = 5.411$ Å, which is in agreement with the JCPDS file for CeO_2 (JCPDS 34-394). Noticeably, in the XRD spectra the highest intensity diffraction peak is located at $2\theta = 28.660^\circ$, which is from the (111) lattice plane of face-centered cubic form of CeO_2 . The abovementioned observation is corroborated with the interplanar spacing of the (111) plane, as calculated from the HRTEM image. Figure 1D divulges the chemical fingerprints of pristine ceria. In the Fourier-transform infrared (FTIR) spectrum of pristine CeO_2 , the broad intense band at around 3425 cm^{-1} corresponds to the O–H stretching vibration of adsorbed water and hydroxyl groups on the nanoparticle surface (Ce–H), whereas the peak at 1628 cm^{-1} arises because of the scissor bending of internally bonded water molecules.²⁴ The peak at 1384 cm^{-1} represents the N–O stretch because of the residual presence of nitrate.²⁵ The intense absorption band in the low wave-number region (600 – 500 cm^{-1}), as well as the small peak at around 850 cm^{-1} , are the characteristics of Ce–O vibrations.²⁶

Viability of HCT 116 Colon Cancer Cell Line. Exposure to CeO_2 at different concentrations (5 , 10 , 20 , 40 , 60 , 80 , and 100 $\mu\text{g}/\text{mL}$) led to cell death with a significantly lower IC_{50} of 50.48 $\mu\text{g}/\text{mL}$, as compared to the relatively toxic anticancer drug. At a dose of 28.12 and 72.86 $\mu\text{g}/\text{mL}$, 30 and 70% of cell deaths were observed, respectively (Figure 2). Thus, three

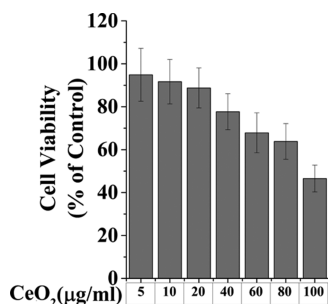


Figure 2. Nanoceria dose-dependent viability of HCT 116 colorectal carcinoma cell line (after 24 h).

concentrations (30 , 50 , and 70 $\mu\text{g}/\text{mL}$) on the basis of IC_{30} , IC_{50} , and IC_{70} were chosen for the entire study to evaluate the molecular mechanism of action. For comparison with normal (noncancerous) cell line, we have studied the cytotoxicity of CeO_2 in the human embryonic kidney (HEK 293) cell line by an MTT assay after 24 h of treatment (Figure S1 in the Supporting Information). The results suggest that up to 37 $\mu\text{g}/\text{mL}$ there was almost no cytotoxicity. The calculated value of IC_{50} for HEK 293 cell line was 92.03 $\mu\text{g}/\text{mL}$. In fact, the inhibitory concentrations IC_{30} , IC_{50} , and IC_{70} are substantially

less for HCT 116, as compared to those for HEK 293 cell lines, suggesting that cerium oxide is a potent anticancer agent.

Molecular Mechanisms of CeO_2 -Induced Cellular Apoptosis.

Numerous scientific reports demonstrated that nanoparticle-assisted anticancer activity was guided through the generation of intercellular ROS (iROS). Thus, to evaluate the correlation between anticancer activity and intercellular ROS generation upon CeO_2 treatment, flow cytometric assessment was carried out using ROS-sensitive indicator $\text{H}_2\text{DCF-DA}$ ($2',7'$ -dichlorofluorescein diacetate). A dose-dependent (30 , 50 , and 70 $\mu\text{g}/\text{mL}$) augmentation of DCF fluorescence (DCF+ population) in terms of ROS upon CeO_2 treatment was observed with respect to the control cells, suggesting that CeO_2 -generated ROS could be a potent inducer of cellular death (Figure 3A). CeO_2 -induced cell death was further confirmed by the assessment of apoptosis and necrosis using Annexin V-FITC and DAPI staining. Externalization of phosphatidylserine from lipid bilayer upon cell death is the hallmark indicator of apoptosis as changes in the membrane asymmetry can contribute numerous cellular functions associated with apoptosis. Annexin V binds to phosphatidylserine when it is present on the outer leaflet of the plasma membrane. Flow cytometric analysis revealed that % cell population in early (Annexin V-FITC+ population) and late apoptosis (Annexin V-FITC+/DAPI+ population) was increased markedly with the treatment of CeO_2 in a dose-dependent (30 , 50 , and 70 $\mu\text{g}/\text{mL}$) manner (Figure 3B). A unique feature of the early stages of apoptosis is the disruption of active mitochondrial function that includes changes in the membrane potential and alterations to the oxidation–reduction potential of the mitochondria.²⁷ Thus, to validate the CeO_2 -induced apoptosis was associated with the modification of mitochondrial membrane potential (MMP); JC-1 was used to detect the changes in mitochondrial health in terms of potential difference. JC-1, a membrane-permeant dye, exhibits potential-dependent accumulation in mitochondria which is indicated by a decrease in the red/green fluorescence intensity.²⁸ Ceria treatment markedly increased the JC-1 green fluorescence intensity in a dose-dependent manner with respect to the control cells (Figure 3C). The maximum change in JC-1 red/green fluorescence intensity ratio was found when cells were treated with 70 $\mu\text{g}/\text{mL}$ of CeO_2 (Figure 3C). The data suggested that CeO_2 treatment could alter the MMP following the induction of apoptotic machinery. Apoptosis is an intricate mechanism for programmed cell death and is associated with the modulation of plethora of cellular signaling proteins. Earlier reports demonstrated that two types of proteins, especially antiapoptotic Bcl2 family of proteins regulate apoptosis by controlling mitochondrial permeability that resides in the outer mitochondrial wall inhibiting cytochrome c release.²⁹ The other proteins, namely pro-apoptotic Bax and Bak which lie in the cytosol but translocate to mitochondria following the stress signaling, where they promote the release of cytochrome c from the mitochondria.^{30,31} Upon liberation from mitochondria, cytochrome c binds to Apaf-1 and forms an activation complex with caspase-9 which further recruits and cleaves caspase-9 and caspase-3.³² The sequential activation of caspases allows running execution-phase of cell apoptosis through the cleavage of other regulatory proteins.^{33,34}

To justify whether the mechanism of apoptosis upon CeO_2 treatment was mitochondrial dependent or not, flow cytometric evaluation of protein expression was conducted.

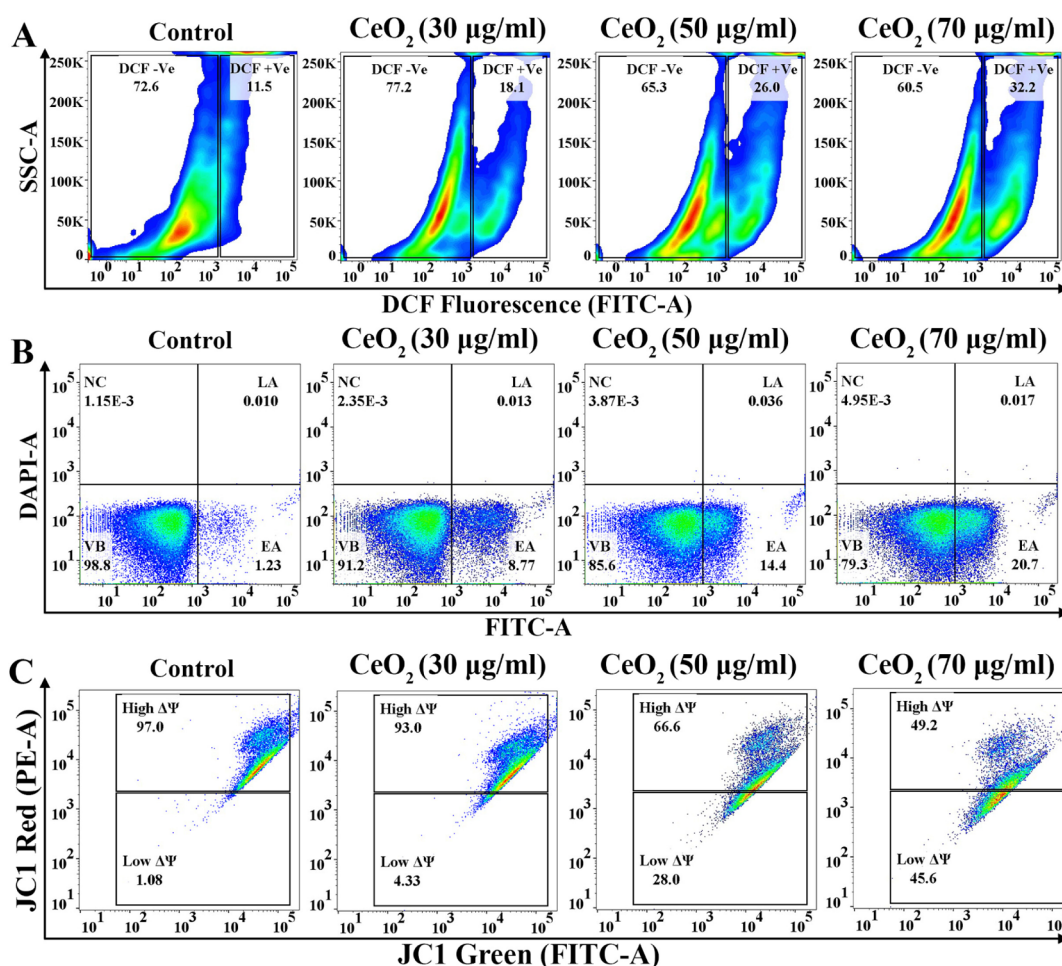


Figure 3. (A) ROS level of 30, 50, and 70 μg/mL CeO₂-treated HCT 116 cells after 24 h; (B) flow cytometric analysis of Annexin V-FITC/DAPI-binding levels of 30, 50, and 70 μg/mL CeO₂-treated HCT 116 cells after 24 h; (C) dose-dependent change in MMP with 30, 50, and 70 μg/mL CeO₂-treated HCT 116 cells after 24 h.

An enhanced relative fluorescence intensity of Bax-FITC (Figure 4A), Bak-FITC (Figure 4C), and cytochrome *c*-FITC (Figure 4D) were found when the cells were treated with CeO₂ in a dose-dependent manner. On the other hand, the antiapoptotic protein Bcl2 was markedly decreased as well (Figure 4B), indicating the imbalance between pro- and antiapoptotic protein expressions that could facilitate the apoptotic burden.

The results also demonstrated that the apoptotic load was executed finally in the activation of caspase as CeO₂ treatment markedly enhanced the caspase-3 and caspase-9 activity in graded doses (30, 50, and 70 μg/mL), while it was gradually decreased with the co-treatment of caspase inhibitor, Z-VAD-FMK (Figure 4E). A growing body of evidence suggested that mitochondrial-dependent apoptosis is typically initiated by DNA damage which further modulates cellular redox status associated with the cell death mechanism.^{35,36} Histone H2AX phosphorylated on serine 139 (γ -H2AX), one of the hallmarks of DNA damage and DNA double-strand breaks (DSB), is modulated through iROS. Thus, to assess the role of CeO₂ in the induction of DNA damage, immunofluorescence study was carried out to detect the phosphorylation of γ -H2AX underlying the foci formation in the nucleus. A significant number of γ -H2AX foci were located when the cells were treated with 50 μg/mL of CeO₂ (IC₅₀) which was further increased in 70 μg/mL of treatment (IC₇₀) (Figure 5). These

data confirmed that CeO₂ could involve the apoptosis mechanism through the phosphorylation of γ -H2AX. The primary DSB indicator, γ -H2AX, further activates one of the major redox-assisted transcription factor, p53, that is involved in the regulation of DNA repair to allow the lesions to be repaired or lead to programmed cell death. In cytoplasm, the activity of p53 is masked through the inhibitory action of Mdm2 which act as a negative regulator and functions as a ubiquitin ligase.³⁷ Upon DNA damage, phosphorylation of p53 disrupts the Mdm2 binding, and the inhibitory masking is withdrawn following the nuclear translocation.³⁸ In particular, p53 enhances p21 transcription in the nucleus, which in turn inhibits cyclin-dependent kinase activity followed by the prevention of pRb from derepressing E2F1 which suppress the progression from G1 to S phase.³⁹ The current study revealed that the expression of Mdm2 was suppressed when the cells were treated with CeO₂ in a dose-dependent manner as evident from a gradual decrease in AF488 relative fluorescence intensity (Figure 5), supporting the fact that CeO₂ triggered the disruption of Mdm2 from p53 upon the phosphorylation of γ -H2AX.^{40,41} On one hand, a gradual increase in the phosphorylation of p53 was also evidently correlating the hypothesis underlying the role CeO₂-induced disruption of Mdm2 which further induced the nuclear translocation of p53 as CeO₂ treatment enhanced the p-p53-FITC fluorescence intensity in the nucleus (Figure 6).

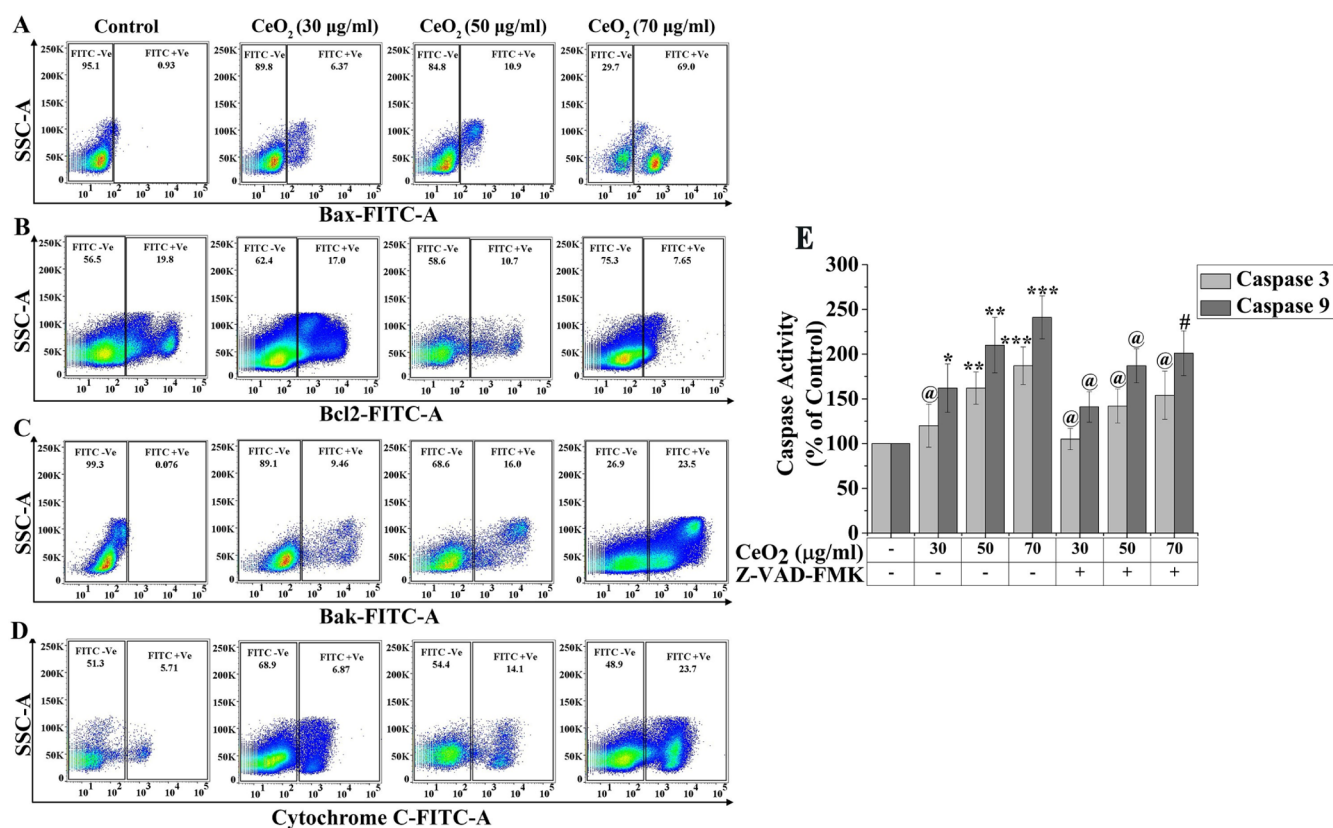


Figure 4. (A) Level of Bax; (B) Bcl2; (C) Bak; (D) cytochrome c positive cells; (E) dose-dependent level of active caspase 3 and active caspase 9 after treatment with CeO₂ nanoparticles with and without Z-VAD-FMK.

Furthermore, it is apparent from Figure 6 that phosphorylation of p53 also elicited the p21 activation as CeO₂ treatment markedly increased the p21 expression as well as the colocalization with p53, indicating that CeO₂-induced phosphorylation of p53 activated two pathways, DNA repair along with apoptosis.⁴² The results also showed that CeO₂ treatment markedly increased nuclear fragmentation as evident from altered comet indices (Figure 7). The ROS-induced DNA damage was also confirmed by the DNA fragmentation assay (Figure S2 in the Supporting Information). The data suggested that DNA fragmentation was increased in a CeO₂ dose-dependent manner. Biochemical events leading to the apoptotic changes include blebbing, cell shrinkage, nuclear fragmentation, chromatin condensation, and chromosomal DNA fragmentation which confirmed the observed data that CeO₂ treatment may modulate apoptosis through the p53-dependent mitochondrial-assisted pathway (Figure 8).

CONCLUSIONS

The present study has shown that CeO₂ nanoparticles inhibit the proliferation of colon cancer cells (HCT 116) in a dose-dependent manner and can induce apoptosis through the generation of intercellular ROS. Interestingly, for normal cells such as HEK 293 cell line, a significantly reduced cytotoxicity is observed. Furthermore, CeO₂-induced apoptosis could be correlated with alteration of MMP, caspase activation, and chromosomal DNA fragmentation. Nanoceria has been found as a bona fide anticancer agent that acts in a p53-dependent manner. In the future, pristine CeO₂ nanoparticles, or those conjugated with the specified antibody or anticancer drugs,

may be applied for colon cancer therapy, without the adverse effects rendered by the conventional chemotherapeutic drugs.

MATERIALS AND METHODS

Materials. Cerium(III) nitrate hexahydrate [Ce(NO₃)₃·6H₂O, 99%], ethylene glycol (EG, 99.8%), and (3-aminopropyl)triethoxysilane (≥98% pure) were procured from Sigma-Aldrich (Germany) and were used without further purification. The solutions were prepared using deionized (DI) water from Milli-Q Direct Water Purification System (Merck Millipore, Billerica, MA, USA).

HCT 116 and HEK 293 cell lines were obtained from NCCS Pune, India. Dulbecco's modified Eagle medium (DMEM), fetal bovine serum (FBS), penicillin streptomycin neomycin (PSN) antibiotic, trypsin, and ethylenediaminetetraacetic acid (EDTA) were obtained from Gibco BRL (Grand Island, NY, USA). Tissue culture plastic wares were purchased from NUNC (Roskilde, Denmark). 3-(4,5-Dimethylthiazol-2-yl)-2,5-diphenyltetrazolium bromide (MTT), 4',6-diamidino-2-phenylindole (DAPI), and ethidium bromide (EtBr) were purchased from SRL (India). Antibodies and all other chemicals used were procured from Sigma-Aldrich (St. Louis, MO, USA).

Synthesis of Cerium Oxide Nanoparticles. Cerium oxide nanoparticles were synthesized using EG-assisted ammonia-induced precipitation method. Briefly, 7.8 mL EG was added to 92.2 mL of DI water in a 250 mL of two-neck round bottom flask at 50 °C in a silicone bath reflux condenser system and kept under constant stirring at 350 rpm. Subsequently, 5.16 g of cerium nitrate was added into the EG/water solution at a molar ratio of 10:1. After complete

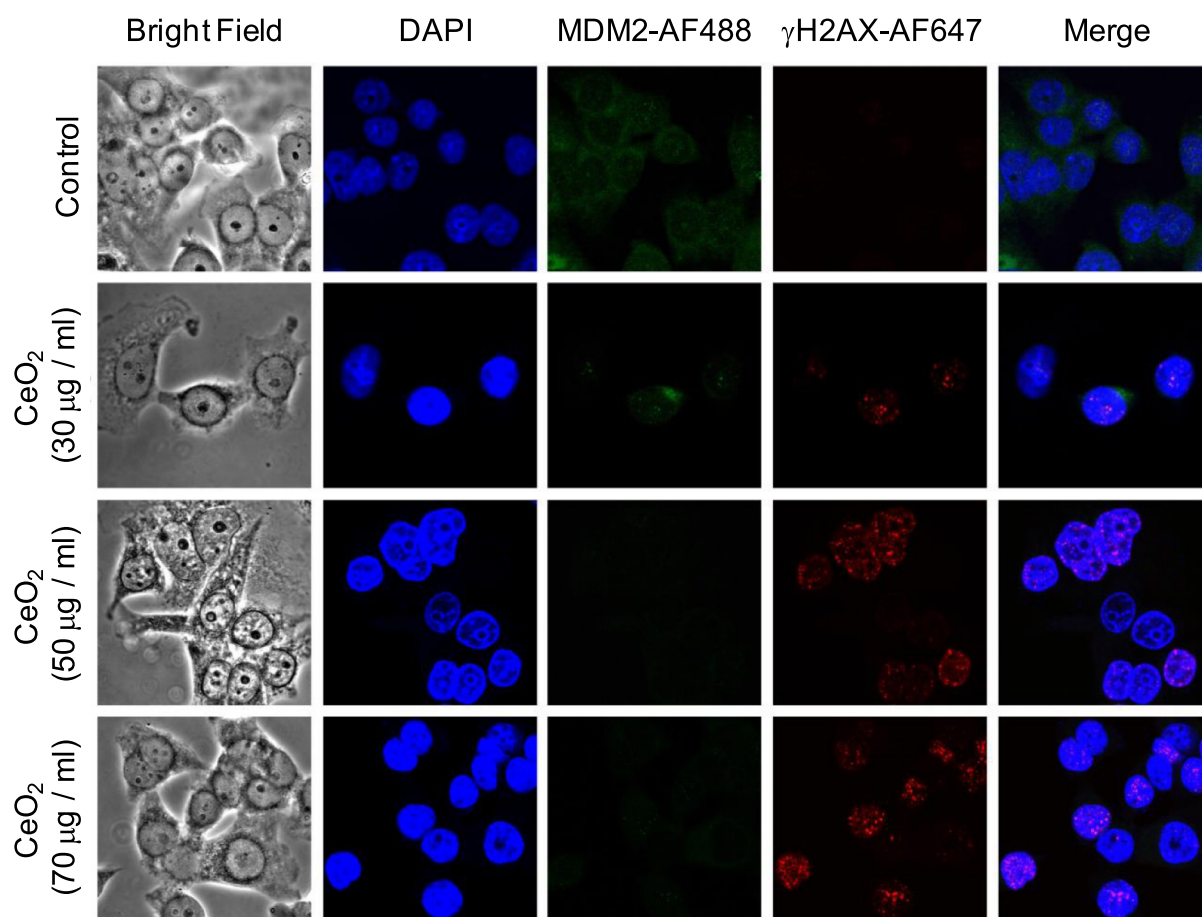


Figure 5. Localization of Mdm2 and generation of γ -H2AX foci after treatment of CeO₂ at 30, 50, and 70 μ g/mL of HCT 116 by confocal microscopy.

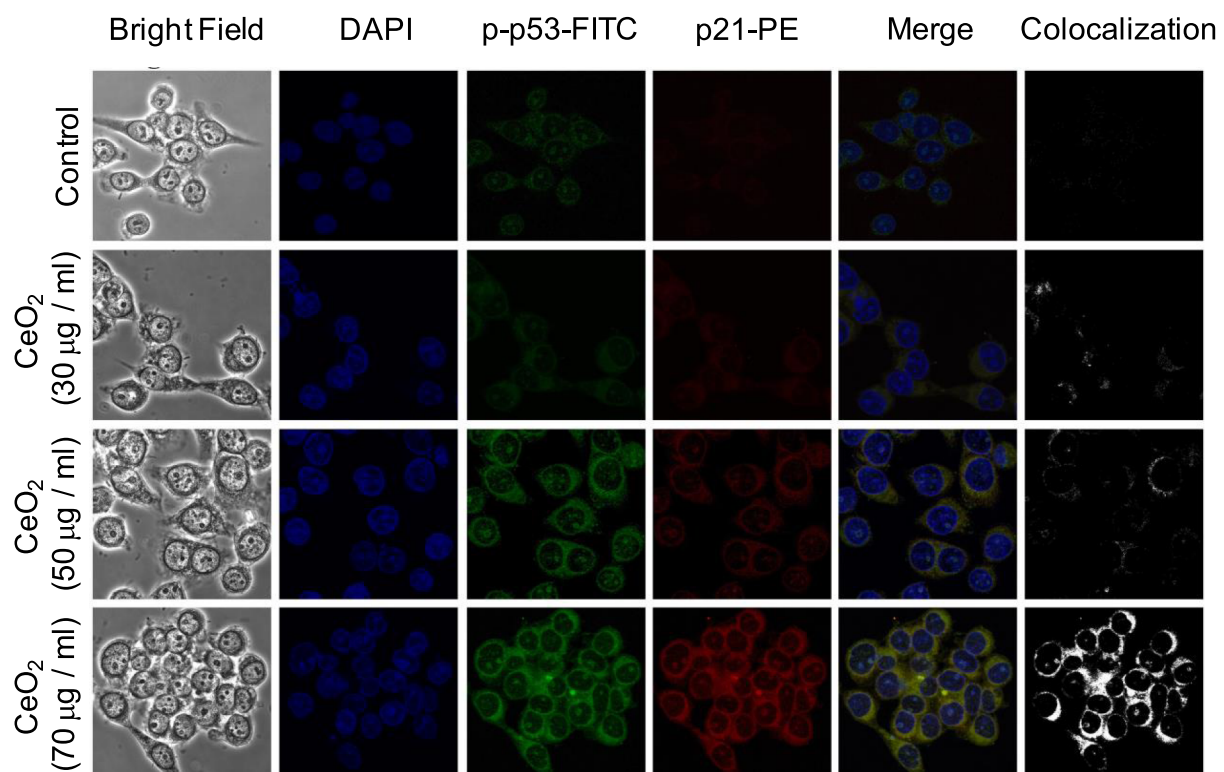


Figure 6. Localization of p53 and p21 after treatment of CeO₂ at 30, 50, and 70 μ g/mL of HCT 116 by confocal microscopy.

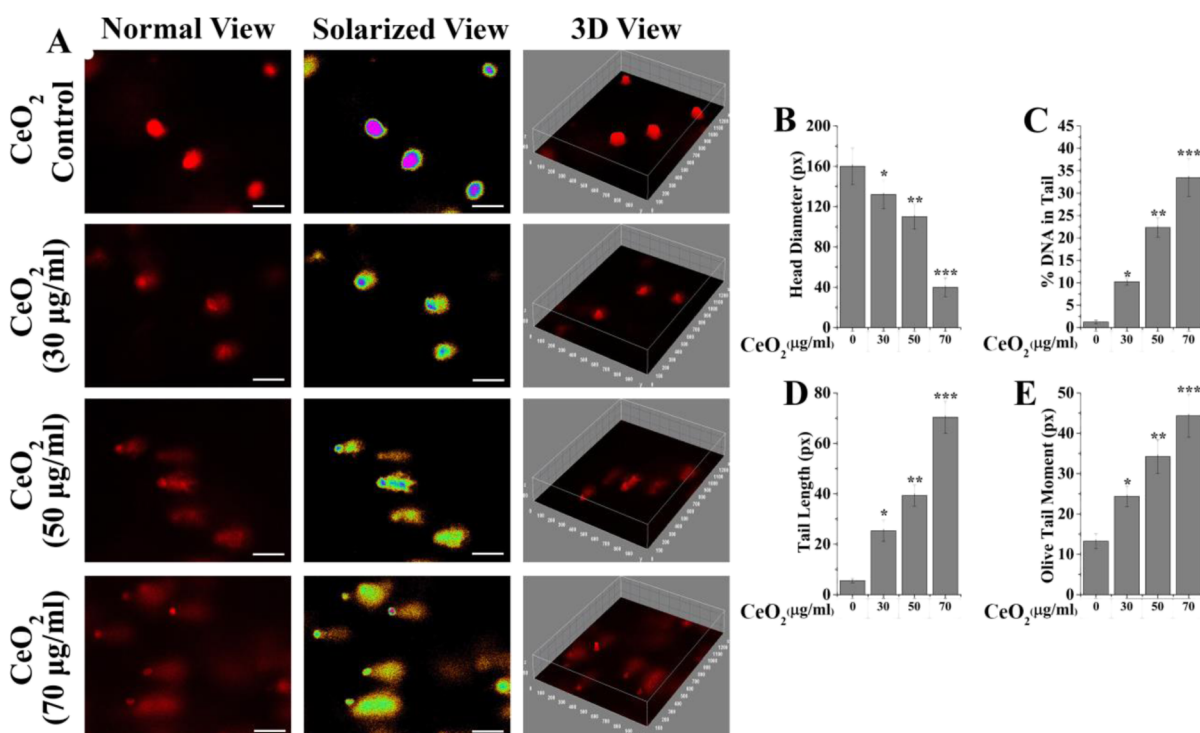


Figure 7. (A) Comet assay results after incubation of HCT 116 cells with treatment of CeO₂ at 30, 50, and 70 µg/mL; (B) head diameter, (C) % DNA in tail, (D) tail length; and (E) olive tail moment.

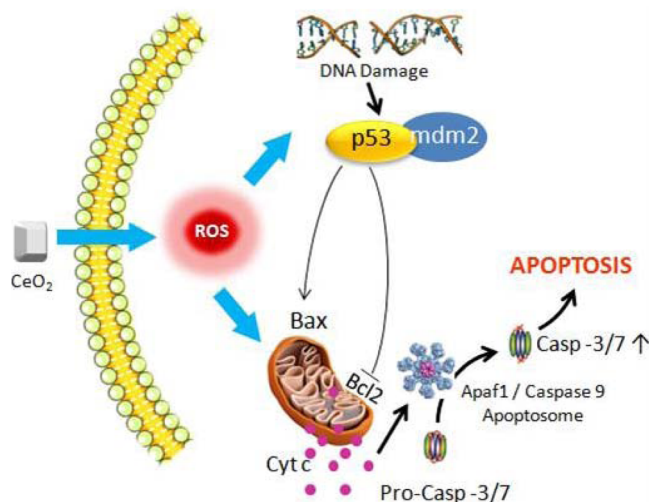


Figure 8. Plausible mechanism of CeO₂-induced apoptosis of human colon cancer cells (HCT 116) by ROS-generated mitochondrial-mediated pathway.

dissolution of cerium nitrate, 5 mL of aqueous ammonia was added to the solution, and the pH was adjusted to 9.6. The solution was kept under constant magnetic stirring at 750 rpm until the color of the solution turned yellowish, which indicated formation of cerium oxide. Subsequently, the solution was subjected to vacuum filtration using Whatman ($\varnothing = 110$ mm and grade 589/3) filter paper, washed alternately with ethanol and DI water, and dried overnight under vacuum. Finally, the as-synthesized materials were calcined at 400 °C for 2 h to obtain phase-pure CeO₂ nanoparticles.

Characterization of the Nanoparticles. The morphology of the prepared ceria nanoparticles was characterized by

TEM using a JEOL JEM 2100 high resolution transmission electron microscope. Nitrogen adsorption and desorption isotherms at 77 K were measured using a NOVA 4000E Surface Area Analyzer system (Quantachrome Instruments, FL, USA). The samples were pretreated at 300 °C for 2 h under vacuum. Data analysis was performed using NOVAwin software (version 10.01). Zeta potential (ζ), the overall surface charge of the nanoparticles in solution (~ 1 mg/mL in DI water at pH 7.4) was assessed by an electrophoretic light scattering Zetasizer Nano ZS zeta potential analyzer (Malvern Instruments Ltd, Malvern, UK). FTIR spectroscopy using an IRPrestige-21 spectrophotometer (Shimadzu Corporation, Tokyo, Japan) was performed to substantiate the presence of reactive amino silane moieties on the modified metal-oxide surface. An X-ray diffractometer (Rigaku Ultima III, Tokyo, Japan) determined the phase analysis of the nanoparticles, carried out using Cu K α radiation ($\lambda = 0.15418$ nm) in a continuous scan mode from 20 to 80° at a scan speed of 1°/min.

Cell Culture. HCT 116 and HEK 293 cell lines were independently cultured in DMEM with 10% FBS and 1% PSN antibiotic mixture at 37 °C in a humidified atmosphere under 5% CO₂. After 75–80% confluence, cells were harvested with 0.52 mM EDTA and 0.25% trypsin in phosphate buffered saline (PBS) and seeded at required density to allow them to re-equilibrate for a day before starting the experiment.

Cell Viability Assays. For defining the cell viability, an MTT assay was performed. For the initial screening, HCT 116 or HEK 293 cells were seeded (4×10^3 cells per well) in 96 well plate and maintained at 37 °C in a humidified 5% CO₂ atmosphere. Cell viability was assessed by treatment of CeO₂ at different concentrations (5, 10, 20, 40, 60, 80, and 100 µg/mL). Nanoparticle-treated plates were kept in an incubator for 24 h, following which the cells were washed with PBS.

Subsequently, MTT solution (4 mg/mL in PBS) was added in each well and kept in the incubator for 4 h. Absorbance of the solubilized intracellular formazan was calculated at 595 nm using an ELISA reader (EMax, Molecular Devices LLC, San Jose, CA, USA). In all cases, the nanoparticle suspensions were sonicated before being added to the cell culture to obtain homogenized mixtures. The cell culture assays were repeated in triplicate at the desired concentrations.

Quantification of Apoptosis Using Annexin V-FITC. Apoptosis was assayed through the use of an Annexin V-FITC apoptosis detection kit (Calbiochem, CA, USA). After treating with CeO₂ nanoparticles (30, 50, and 70 μg/mL as per IC₃₀, IC₅₀, and IC₇₀, respectively) for 24 h, the cells were washed and stained with Annexin V-FITC, which is in accordance with the manufacturer's instructions. The percentages of live, apoptotic, and necrotic cells were evaluated by flow cytometry (BD LSRFortessa, San Jose, CA, USA).

Measurement of MMP. For measuring MMP, cells were treated with CeO₂ (30, 50, and 70 μg/mL as per IC₃₀, IC₅₀, and IC₇₀, respectively) for 24 h and then incubated with JC-1 (5,5',6,6'-tetrachloro-1,1',3,3'-tetraethylbenzimidazolylcarbocyanine iodide, Sigma) at 37 °C, 5% CO₂ for 30 min. After incubation, centrifugation was carried out at 400g for 5 min at room temperature, and the supernatant was removed. Then, the cell pellets were suspended in 500 μL PBS. Data from 10⁶ cells were analyzed in a BD LSRFortessa (San Jose, CA, USA) cell analyzer for each sample. For healthy cells, having high MMP, the reagent gives fluorescence in the FITC channel for green monomers, as compared to apoptotic cells, indicating a significant drop in the MMP resulting in PE-Texas Red A channel for dead aggregates.

Measurement of Intracellular ROS. Mitochondria are the major sites of ROS production in mammalian cells, and superoxide (O₂⁻) seems to be the primary ROS produced as the result of single electron reduction of O₂. ROS plays an important role in the motivation of apoptosis in a variety of cells. For measuring the ROS generation, cells were treated with CeO₂ (30, 50, and 70 μg/mL as per IC₃₀, IC₅₀, and IC₇₀, respectively) for 24 h and incubated with 10 μM of H2DCFDA at 37 °C for 25 min, and then, cells were analyzed by flow cytometry. The increase in fluorescence because of production of ROS was noted by a flow cytometer (BD LSRFortessa, San Jose, CA, USA). For data of each sample, 1 × 10⁶ cells were analyzed.

Caspase-3 and Caspase-9 Activity Assays. HCT 116 cells were treated with CeO₂ (30, 50, and 70 μg/mL as per IC₃₀, IC₅₀, and IC₇₀, respectively) for 24 h, and caspase-3 and caspase-9 activities were quantified with the commercially available caspase-3 and caspase-9 colorimetric assay kit (BioVision Research Products, Mountain View, CA), respectively. Caspase activities were detected at 405 nm by a spectrophotometer on an ELISA reader.

Analysis of Protein Expression by Flow Cytometry. After treatment with CeO₂ (30, 50, and 70 μg/mL as per IC₃₀, IC₅₀, and IC₇₀, respectively) fixation of cells was carried out by 4% paraformaldehyde in PBS (pH 7.4) for 20 min at room temperature. 0.1% Triton X-100 in PBS was used for permeabilization with 0.1% FBS for 5 min. After washing twice with PBS with 3% FBS, the permeabilized cells were incubated with primary antibody on ice for 2 h and washed with PBS. Then, the cells were incubated with FITC-conjugated goat anti-rabbit IgG as secondary antibody for 2 h on ice and washed twice with PBS. The stained cells were

acquired and analyzed using a BD LSRFortessa flow cytometer (San Jose, CA, USA) equipped with FlowJo software.

Confocal Microscopy. Briefly, after treatment with CeO₂, the cover slips containing HCT 116 cells were washed twice for 10 min each in 0.01 M PBS and incubated for 1 h in blocking solution containing 2% normal bovine serum and 0.3% Triton X-100 in PBS. After blocking, the slides were incubated overnight at 4 °C with the proper primary antibody. Fluorophore-conjugated secondary antibodies were diluted 1:100 in the blocking solution and incubated for 2 h. The slides were then counterstained with DAPI for 10 min and mounted with the ProLong Anti-fade Reagent (Molecular Probe, Eugene, OR, USA). Staining images of the double immunofluorescence were examined using a confocal laser-scanning microscope (FV 10i, Olympus, Japan).

Assessment of Nuclear DNA Damage Using Single Cell Gel Electrophoresis Assay. The oxidative DNA damage was measured by performing the comet assay. The CeO₂-treated cells were mixed with 100 μL of 0.5% low melting agar (LMA) at 39 °C and then spread on a fully frosted microscopic slide precoated with 200 μL of 1% LMA. After agarose solidification, the slide was covered with 75 μL of 0.5% LMA and immersed in lysis solution (2.5 M NaCl, 100 mM Na-EDTA, 10 mM Tris, 1% Triton X-100 and 10% DMSO, pH 10) for 1 h at 4 °C. The slides were employed in a gel-electrophoresis apparatus containing 300 mM NaOH and 10 mM Na-EDTA (pH 13) for 40 min to allow DNA unwinding and the expression of alkali-labile damage. An electrical field was applied (300 mA, 25 V) for 20 min at 4 °C to draw negatively charged DNA toward the anode. After electrophoresis, the slides were washed three times for 5 min at 4 °C in a neutralizing buffer (0.4 M Tris pH 7.5) and then stained with 75 μL EtBr solution (20 mg/mL). The slides were photographed using a fluorescence microscope, and the images were analyzed by CometScore software (v1.5).

■ ASSOCIATED CONTENT

SI Supporting Information

The Supporting Information is available free of charge at <https://pubs.acs.org/doi/10.1021/acsomega.9b04006>.

Nanoceria dose-dependent viability of HEK 293 cell line and CeO₂-induced DNA fragmentation in HCT 116 cells (PDF)

■ AUTHOR INFORMATION

Corresponding Author

Aparna Datta – School of Materials Science and Nanotechnology, Jadavpur University, Kolkata 700032, West Bengal, India; orcid.org/0000-0003-2246-0107; Email: adatta.research@gmail.com

Authors

Snehasis Mishra – Cancer Biology and Inflammatory Disorder Division, CSIR-Indian Institute of Chemical Biology, Kolkata 700032, West Bengal, India

Krishnendu Manna – Cancer Biology and Inflammatory Disorder Division, CSIR-Indian Institute of Chemical Biology, Kolkata 700032, West Bengal, India

Krishna Das Saha – Cancer Biology and Inflammatory Disorder Division, CSIR-Indian Institute of Chemical Biology, Kolkata 700032, West Bengal, India

Siddhartha Mukherjee – Department of Metallurgical and Material Engineering, Jadavpur University, Kolkata 700032, West Bengal, India

Somenath Roy – CSIR-Central Glass and Ceramic Research Institute, Kolkata 700032, West Bengal, India; orcid.org/0000-0002-3352-0534

Complete contact information is available at:
<https://pubs.acs.org/10.1021/acsomega.9b04006>

Author Contributions

A.D. and S. M. contributed equally. All authors have given approval to the final version.

Notes

The authors declare no competing financial interest.

ACKNOWLEDGMENTS

Research fellowship and research associateship from DST-SERB, Govt. of India, awarded to S.M. and K.M., respectively, are gratefully acknowledged. The authors are thankful to Binayak Paul and Banasri Das for providing technical assistance for confocal microscopy. The authors are also grateful to Tanmoy Dalui and Deblina Mukherjee for generous assistance in flow cytometry. The funding agency had no role in the design of the study; in the collection, analyses, or interpretation of data; and in the writing of the manuscript.

REFERENCES

- (1) Thyagarajan, A.; Sahu, R. P. Potential contributions of antioxidants to cancer therapy: immunomodulation and radiosensitization. *Integr. Cancer Ther.* **2018**, *17*, 210–216.
- (2) Chio, I. I. C.; Tuveson, D. A. ROS in cancer: The burning question. *Trends Mol. Med.* **2017**, *23*, 411–429.
- (3) Ambrosone, C. B.; Zirpoli, G. R.; Hutson, A. D.; McCann, W. E.; McCann, S. E.; Barlow, W. E.; Kelly, K. M.; Cannioto, R.; Sucheston-Campbell, L. E.; Hershman, D. L.; Unger, J. M.; Moore, H. C. F.; Stewart, J. A.; Isaacs, C.; Hobday, T. J.; Salim, M.; Hortobagyi, G. N.; Gralow, J. R.; Budd, G. T.; Albain, K. S. Dietary supplement use during chemotherapy and survival outcomes of patients with breast cancer enrolled in a cooperative group clinical trial. *J. Clin. Oncol.* **2019**, *38*, 804.
- (4) Wang, J.; Luo, B.; Li, X.; Lu, W.; Yang, J.; Hu, Y.; Huang, P.; Wen, S. Inhibition of cancer growth in vitro and in vivo by a novel ROS-modulating agent with ability to eliminate stem-like cancer cells. *Cell Death Dis.* **2017**, *8*, No. e2887.
- (5) Stone, W. L.; Krishnan, K.; Campbell, S. E.; Palau, V. E. The role of antioxidants and pro-oxidants in colon cancer. *World J. Gastrointest. Oncol.* **2014**, *6*, 55–66.
- (6) Pathak, R. K.; Kolishetti, N.; Dhar, S. Targeted nanoparticles in mitochondrial medicine. *Wiley Interdiscip. Rev.: Nanomed. Nanobiotechnol.* **2015**, *7*, 315–329.
- (7) Pinto, M. P.; Arce, M.; Yameen, B.; Vilos, C. Targeted brain delivery nanoparticles for malignant gliomas. *Nanomedicine* **2017**, *12*, 59–72.
- (8) Korsvik, C.; Patil, S.; Seal, S.; Self, W. T. Superoxide dismutase mimetic properties exhibited by vacancy engineered ceria nanoparticles. *Chem. Commun.* **2007**, 1056–1058.
- (9) Fisher, T. J.; Zhou, Y.; Wu, T.-S.; Wang, M.; Soo, Y.-L.; Cheung, C. L. Structure–activity relationship of nanostructured ceria for the catalytic generation of hydroxyl radicals. *Nanoscale* **2019**, *11*, 4552–4561.
- (10) Pirmohamed, T.; Dowding, J. M.; Singh, S.; Wasserman, B.; Heckert, E.; Karakoti, A. S.; King, J. E. S.; Seal, S.; Self, W. T. Nanoceria exhibit redox state-dependent catalase mimetic activity. *Chem. Commun.* **2010**, *46*, 2736–2738.
- (11) Patel, V.; Singh, M.; Mayes, E. L. H.; Martinez, A.; Shutthanandan, V.; Bansal, V.; Singh, S.; Karakoti, A. S. Ligand-mediated reversal of the oxidation state dependent ROS scavenging and enzyme mimicking activity of ceria nanoparticles. *Chem. Commun.* **2018**, *54*, 13973–13976.
- (12) Tian, Z.; Li, J.; Zhang, Z.; Gao, W.; Zhou, X.; Qu, Y. Highly sensitive and robust peroxidase-like activity of porous nanorods of ceria and their application for breast cancer detection. *Biomaterials* **2015**, *59*, 116–124.
- (13) Liu, Q.; Yang, Y.; Lv, X.; Ding, Y.; Zhang, Y.; Jing, J.; Xu, C. One-step synthesis of uniform nanoparticles of porphyrin functionalized ceria with promising peroxidase mimetics for H₂O₂ and glucose colorimetric detection. *Sens. Actuators, B* **2017**, *240*, 726–734.
- (14) Kim, H. Y.; Ahn, J. K.; Kim, M. I.; Park, K. S.; Park, H. G. Rapid and label-free, electrochemical DNA detection utilizing the oxidase-mimicking activity of cerium oxide nanoparticles. *Electrochem. Commun.* **2019**, *99*, 5–10.
- (15) Celardo, I.; De Nicola, M.; Mandoli, C.; Pedersen, J. Z.; Traversa, E.; Ghibelli, L. Ce³⁺ Ions Determine Redox-Dependent Anti-apoptotic Effect of Cerium Oxide Nanoparticles. *ACS Nano* **2011**, *5*, 4537–4549.
- (16) Zeng, F.; Wu, Y.; Li, X.; Ge, X.; Guo, Q.; Lou, X.; Cao, Z.; Hu, B.; Long, N. J.; Mao, Y.; Li, C. Custom-Made Ceria Nanoparticles Show a Neuroprotective Effect by Modulating Phenotypic Polarization of the Microglia. *Angew. Chem., Int. Ed.* **2018**, *57*, 5808–5812.
- (17) Kim, C. K.; Kim, T.; Choi, I.-Y.; Soh, M.; Kim, D.; Kim, Y.-J.; Jang, H.; Yang, H.-S.; Kim, J. Y.; Park, H.-K.; Park, S. P.; Park, S.; Yu, T.; Yoon, B.-W.; Lee, S.-H.; Hyeon, T. Ceria nanoparticles that can protect against ischemic stroke. *Angew. Chem., Int. Ed.* **2012**, *51*, 11039–11043.
- (18) Lin, W.; Huang, Y.-w.; Zhou, X.-D.; Ma, Y. Toxicity of Cerium Oxide Nanoparticles in Human Lung Cancer Cells. *Int. J. Toxicol.* **2006**, *25*, 451.
- (19) De Marzi, L.; Monaco, A.; De Lapuente, J.; Ramos, D.; Borras, M.; Di Gioacchino, M.; Santucci, S.; Poma, A. Cytotoxicity and Genotoxicity of Ceria Nanoparticles on Different Cell Lines in Vitro. *Int. J. Mol. Sci.* **2013**, *14*, 3065–3077.
- (20) Mittal, S.; Pandey, A. K. Cerium Oxide Nanoparticles Induced Toxicity in Human Lung Cells: Role of ROS Mediated DNA Damage and Apoptosis. *BioMed Res. Int.* **2014**, *2014*, 891934.
- (21) Wason, M.; Lu, H.; Yu, L.; Lahiri, S.; Mukherjee, D.; Shen, C.; Das, S.; Seal, S.; Zhao, J. Cerium oxide nanoparticles sensitize pancreatic cancer to radiation therapy through oxidative activation of the JNK apoptotic pathway. *Cancers* **2018**, *10*, 303.
- (22) Wason, M. S.; Colon, J.; Das, S.; Seal, S.; Turkson, J.; Zhao, J.; Baker, C. H. Sensitization of pancreatic cancer cells to radiation by cerium oxide nanoparticle-induced ROS production. *Nanomedicine* **2013**, *9*, 558–569.
- (23) Shamim, U.; Hanif, S.; Albanyan, A.; Beck, F. W. J.; Bao, B.; Wang, Z.; Banerjee, S.; Sarkar, F. H.; Mohammad, R. M.; Hadi, S. M.; Azmi, A. S. Resveratrol-induced apoptosis is enhanced in low pH environments associated with cancer. *J. Cell. Physiol.* **2012**, *227*, 1493–1500.
- (24) Huang, X.; Li, L.; Li, G. Synthesis of CeO₂ assemblies through interaction with short-chain dicarboxylic acids under facile hydrothermal conditions. *RSC Adv.* **2019**, *9*, 28581–28587.
- (25) Stodt, M. F. B.; Gonchikzhapov, M.; Kasper, T.; Fritsching, U.; Kiefer, J. Chemistry of iron nitrate-based precursor solutions for spray-flame synthesis. *Phys. Chem. Chem. Phys.* **2019**, *21*, 24793–24801.
- (26) Padmanathan, N.; Selladurai, S. Shape controlled synthesis of CeO₂ nanostructures for high performance supercapacitor electrodes. *RSC Adv.* **2014**, *4*, 6527–6534.
- (27) Qi, G.; Li, H.; Zhang, Y.; Li, C.; Xu, S.; Wang, M.; Jin, Y. smart plasmonicnanorobot for real-time monitoring cytochrome c release and cell acidification in apoptosis during electrostimulation. *Anal. Chem.* **2019**, *91*, 1408–1415.
- (28) Sakamuru, S.; Attene-Ramos, M. S.; Xia, M. Mitochondrial Membrane Potential Assay. *Methods Mol. Biol.* **2016**, *1473*, 17–22.

- (29) Singh, R.; Letai, A.; Sarosiek, K. Regulation of apoptosis in health and disease: the balancing act of BCL-2 family proteins. *Nat. Rev. Mol. Cell Biol.* **2019**, *20*, 175–193.
- (30) Dewson, G.; Kluck, R. M. Mechanisms by which Bak and Bax permeabilise mitochondria during apoptosis. *J. Cell Sci.* **2009**, *122*, 2801–2808.
- (31) Garrido, C.; Galluzzi, L.; Brunet, M.; Puig, P. E.; Didelot, C.; Kroemer, G. Mechanisms of Cytochrome c release from mitochondria. *Cell Death Differ.* **2006**, *13*, 1423–1433.
- (32) Tamura, R.; Takada, M.; Sakaue, M.; Yoshida, A.; Ohi, S.; Hirano, K.; Hayakawa, T.; Hirohashi, N.; Yura, K.; Chiba, K. Starfish Apaf-1 activates effector caspase-3/9 upon apoptosis of aged eggs. *Sci. Rep.* **2018**, *8*, 1611.
- (33) Elena-Real, C. A.; Díaz-Quintana, A.; González-Arzola, K.; Velázquez-Campoy, A.; Orzáez, M.; López-Rivas, A.; Gil-Caballero, S.; De la Rosa, M. A.; Díaz-Moreno, I. Cytochrome c speeds up caspase cascade activation by blocking 14-3-3 ϵ -dependent Apaf-1 inhibition. *Cell Death Dis.* **2018**, *9*, 365.
- (34) Logue, S.; Martin, S. Caspase activation cascades in apoptosis. *Biochem. Soc. Trans.* **2008**, *36*, 1–18.
- (35) Zheng, P.; Chen, Q.; Tian, X.; Qian, N.; Chai, P.; Liu, B.; Hu, J.; Blackstone, C.; Zhu, D.; Teng, J.; Chen, J. DNA damage triggers tubular endoplasmic reticulum extension to promote apoptosis by facilitating ER-mitochondria signaling. *Cell Res.* **2018**, *28*, 833–854.
- (36) Norbury, C. J.; Zhivotovsky, B. DNA damage-induced apoptosis. *Oncogene* **2004**, *23*, 2797–2808.
- (37) García-Cano, J.; Sánchez-Tena, S.; Sala-Gaston, J.; Figueras, A.; Viñals, F.; Bartrons, R.; Ventura, F.; Rosa, J. L. Regulation of the MDM2-p53 pathway by the ubiquitin ligase HERC2. *Mol. Oncol.* **2020**, *14*, 69–86.
- (38) Yadahalli, S.; Neira, J. L.; Johnson, C. M.; Tan, Y. S.; Rowling, P. J. E.; Chattopadhyay, A.; Verma, C. S.; Itzhaki, L. S. Kinetic and thermodynamic effects of phosphorylation on p53 binding to MDM2. *Sci. Rep.* **2019**, *9*, 693.
- (39) Endo, M.; Tanaka, Y.; Otsuka, M.; Minami, Y. E2F1-Ror2 signaling mediates coordinated transcriptional regulation to promote G1/S phase transition in bFGF-stimulated NIH/3T3 fibroblasts. *FASEB J.* **2020**, *34*, 3413.
- (40) Hu, B.; Gilkes, D. M.; Chen, J. Efficient p53 Activation and Apoptosis by Simultaneous Disruption of Binding to MDM2 and MDMX. *Cancer Res.* **2007**, *67*, 8810–8817.
- (41) Sharma, A.; Singh, K.; Almasan, A. Histone H2AX phosphorylation: a marker for DNA damage. *Methods Mol. Biol.* **2012**, *920*, 613–626.
- (42) Abbas, T.; Dutta, A. p21 in cancer: intricate networks and multiple activities. *Nat. Rev. Cancer* **2009**, *9*, 400–414.